Improved diffusion MRI with an ultra-strong gradient head insert

Major Research Project, February 2023.
Flavius-Gabriel Marc, MSc Student, Medical Imaging, Utrecht University, ID: 0862037,
Research intern, Ultra high field MRI: 7-Tesla Group, UMC Utrecht.

Supervisors: dr. ir. Chantal Tax (Examiner), dr. ir. Edwin Versteeg, dr. ir. Jeroen Siero.
Second Reviewer: dr. dr.h.c.mult Alexander Leemans.

***Abstract*—Demyelination and dysmyelination diseases cause damage to the white matter in the central nervous system by disrupting the myelin water sheaths on axons. Diffusion MRI has been suggested to be crucial in uncovering microstructural alterations in white matter. However, conventional diffusion MRI methods are unable to detect myelin water due to its short transverse relaxation time (T2). The use of ultra-strong gradients can significantly shorten the echo time thereby regaining sensitivity to myelin water, but presents technical difficulties including expensive setup and risk of peripheral nerve stimulation. In this work, the potential of using a gradient insert that can be interfaced with existing scanners is assessed to boost diffusion MRI experiments. First, the magnetic force experienced by the cables that supply power to the coil had to be reduced to enable strong diffusion weightings. An optimal cable configuration for the gradient insert coil is presented along with a proposed mechanical design to reduce the magnetic force on cables. This enabled the acquisition of healthy human brain images with strong diffusion weightings. Next, a preprocessing pipeline was developed to address deviations from the imposed diffusion weighting resulting from nonlinearities in the ultra-strong coil's magnetic field, and to correct image distortions resulting from linear eddy currents and susceptibility fields. Finally, the feasibility of quantifying myelin water diffusion with the gradient insert was investigated in simulations.**

I. Introduction

Demyelination and dysmyelination diseases are medical conditions that cause damage to the white matter in the central nervous system. This damage is characterized by lesions that disrupt the myelin coating on axons, leading to the loss of its protective and insulating properties [1].

Nuclear Magnetic Resonance Imaging, also known as MRI, is a method of creating images of soft tissues without invasive procedures. It is highly valued in neurology and neurosurgery due to its ability to accurately diagnose various diseases. In MRI, a powerful magnet (main magnet) generates a strong magnetic field (B0), which aligns the protons in the body. During the acquisition, a radiofrequency (RF) pulse is applied to excite the protons within the body, causing them to temporarily spin out of alignment and resist the pull of the B0 field. When the RF field is turned off, the RF receivers can detect the energy released as the protons return to their original alignment with the main magnetic field. The speed at which the protons realign and the energy released vary based on the chemical nature of the molecules and their environment. These variations are used to construct a detailed image, with contrast showing micro-environmental differences [2].

Gradient coils are an essential part of MRI scanners as they generate a secondary magnetic field, causing a systematic alteration of B0. This provides the ability to encode spatial information of the MR signal, making possible the application of diffusion MRI techniques [3].

Diffusion MRI (dMRI) measures the movement of water molecules in biological tissues [4]. It utilizes gradient fields to identify the thermal-induced random movement of water molecules, thereby providing information at a microscopic level that goes beyond the normal resolution of MRI [5]. The Pulsed Gradient Spin Echo (PGSE) method (Figure 1 below), also known as the Stejskal-Tanner method [6], is the most widely used technique for creating diffusion-weighted (DW) contrast. This involves a pair of RF pulses, consisting of a 90° and 180°, with equally sized gradients positioned on both sides of the 180° pulse. The signal equation for a PGSE experiment is defined as:

$$S = S_0 \exp(-bD) \exp\left(\frac{-TE}{T2}\right), \tag{1}$$

with $S0$ the initial signal intensity with no diffusion weighting, TE is the echo time, and $T2$ is the transverse relaxation time [7]. This equation shows the decline of the spin echo signal, with the signal strength decreasing at an exponential rate as TE increases due to $T2$ relaxation. Additionally, the strength of the signal is influenced by the diffusion of water molecules in the sample, causing a further decline of the signal that directly corresponds to the diffusion coefficient (D). The calculation of apparent diffusion coefficient (ADC) involves fitting the signal model mentioned in equation 1. This is possible when at least two or more b-value images are acquired. b is the diffusion weighting value given by:

$$b = \gamma^2 G^2 \delta^2 \left(\Delta - \frac{\delta}{3}\right), \tag{2}$$

with γ the gyromagnetic ratio, G the gradient amplitude and duration δ, Δ is the time interval, as shown in Figure 1 on the next page [8].

However, conventional diffusion MRI methods are unable to detect myelin water due to its short $T2$. The use of dMRI with strong gradients has been shown to play a crucial role in improving the specificity and sensitivity of microstructural measurements [9][10]. This advanced technique enables the study of diffusion properties at short $T2$ values. Although, strong-gradient imaging presents technical difficulties, including the high cost of setup and the risk of peripheral nerve stimulation.

Futura Composites developed an ultra-strong gradient head insert prototype, designed as an auxiliary piece of equipment.

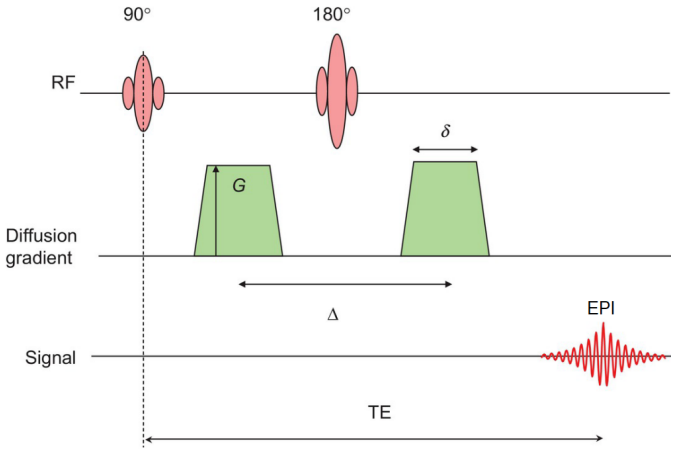


Fig. 1: Typical PGSE sequence with EPI (Echo Planar Imaging) readout for diffusion MRI. Adapted from [8].

This single-axis coil (z-axis) boasts a maximum amplitude gradient strength of 200 mT/m and a maximum slew rate of 1300 T/m/s, resulting in shorter echo times with an increased signal-to-noise ratio (SNR). In order to avoid stimulation of peripheral nerves, the field of view (FOV) of the gradient insert coil was deliberately limited [11]. However, this restriction resulted in a decrease in image quality. Furthermore, the coil had to be adapted for diffusion MRI acquisitions. The application of high currents (greater than 200 A) for DW imaging at high b-values with the gradient insert coil generated a magnetic force on the cables supplying power to the coil. This challenge had to be addressed before conducting the image acquisition.

For the acquisition, a PGSE sequence with EPI readout was used to acquire images of healthy human brain. EPI is beneficial for its high signal-to-noise ratio per unit time, enabling fast acquisition of multiple dMRI image scans. Despite this advantage, EPI is known to have challenges, including its vulnerability to B0 field inhomogeneities and the creation of eddy currents during the fast switch of strong diffusion-weighted gradients. [12].

In this research, an approach for reducing the magnetic force generated by the insertion of the ultra-strong gradient coil into the scanner bore is analyzed. This work also includes a proposal to address this issue in the Discussion section. Additionally, a preprocessing pipeline is implemented to improve the quality of the images and correct deviations in ADC values caused by gradient insert field nonlinearity. Finally, a simulation of an inversion recovery pulse acquisition protocol was conducted, demonstrating the feasibility of modeling diffusion properties at short echo times.

II. Methods

This section begins by discussing the magnetic force and its effect on the gradient insert coil. Next, data acquisition for two different gradient settings is presented. Afterwards, a preprocessing pipeline is proposed to correct for linear eddy currents, susceptibility-induced distortions, and to perform B-matrix correction. The last step in this section presents a simulation aimed at modelling diffusion parameters of myelin water.

A. Experimental Setup with the cables

Initially, the setup with the cables was not meant for DW imaging. The intensity of the current that has to enable the gradient insert coil is higher than 630 A for DW scans, which exceeds the maximum tested current [11]. When testing this setup, it was visible that the cables encounter a magnetic force that can break the connector. The main challenge is limiting this force to stop the motion of the wires and keep the connector intact.

The gradient insert coil is introduced into the main magnet at the scanning time. Part of the cables that supply power to the coil is affected by the magnetic field produced by the main magnet, as shown in Figure 2 on the next page. $\vec{B}$ is the magnetic field produced by the main magnet, and its field lines direction is indicated with dark blue arrows. The sketched light blue rectangle illustrates the bore of the 7T scanner. L is the length (meters) of the cables which interact with the magnetic field $\vec{B}$. When a dedicated amplifier is turned on, current i flows through the cables and reaches the gradient insert coil through the connector. The current is described by moving charges [13] from + to - through the cables represented by red and black lines. For length L of the current-carrying cables, the large magnetic field $\vec{B}$ creates a significant magnetic force $\vec{F_B}$.

This interaction is defined by the Lorentz Force Law [14] and can be written as [15]:

$$\vec{F_B} = iL\vec{B}sin\theta \quad [N] \tag{3}$$

Angle θ represents the angle in degrees between the current i and $\vec{B}$. We assume a uniform magnetic field $\vec{B}$ in the direction illustrated in Figure 2. Since the cables are not perfectly parallel with $\vec{B}$, each will be moved by the magnetic force $\vec{F_B}$ no matter the direction of the current [13]. The magnitude of the force can only be suppressed when θ = 180° or 0° [14].

In addition to the large magnetic field $\vec{B}$, each current-carrying cable produces individual circular loops of magnetic fields in the direction of current i, as shown in Figure 3 on the next page. Those local magnetic fields will act as additive magnetic fields to $\vec{B}$. However, the primary cause of the strong movement of cables is the contribution of $\vec{B}$ when the angle θ is not equal to 180° or 0°. To minimize the movement of cables, it is necessary to arrange them as closely as possible to being parallel with the main magnetic field $\vec{B}$ in region L.

According to equation (3), to reduce the magnetic force $\vec{F_B}$, one can reduce the intensity of the current i, lessen the magnitude of $\vec{B}$ or adjust the angle between the current-carrying cables and $\vec{B}$. The most practical way in this scenario is adjusting the angle, as the magnetic field $\vec{B}$ is fixed at 7T by the main magnet and the current i will always match with the desired gradient waveform to be transmitted by the gradient insert. For this to be achieved, various cable configurations have been tested to minimize the magnetic force.

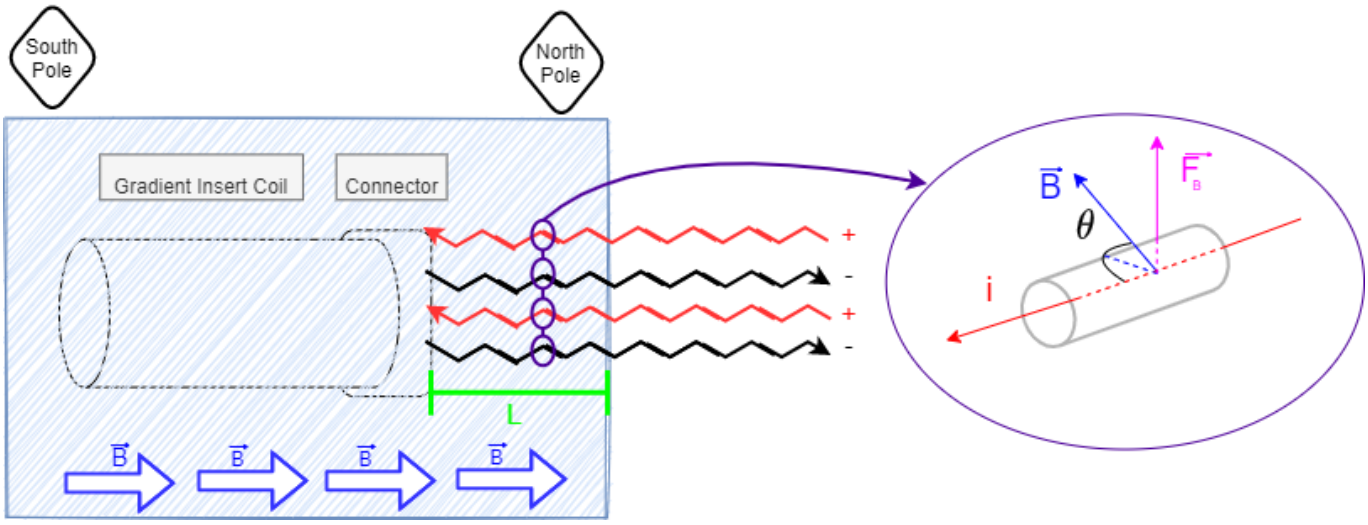


Fig. 2: The magnetic force $\vec{F_B}$ (see the enlarged region for each cable) produced by the magnetic field $\vec{B}$ (generated from the main magnet) when interacting with a current-carrying cable/wire.

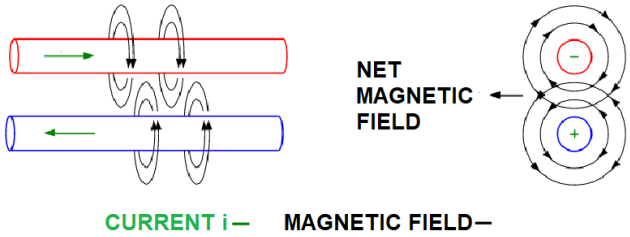


Fig. 3: Circular magnetic fields produced by the current-carrying cables (represented with red and blue cylinders) and the net magnetic field between them. Adapted from [16].

Datasets dMRI	b-values [s/mm^2]	Phase encoding direction	TE [ms]
Gradient insert Slices/Scan: 20	0	RL (right-left)	21,83
	0	LR (left-right)	21,83
	500	RL	28,83
	1000		31,57
	3000		37,73
	6000		43,2
	10000		48,25
Whole-body Slices/Scan: 40	0	RL (right-left)	36,98
	0	LR (left-right)	36,98
	500	RL	62,62
	1000		71,17
	3000		90,98
	6000		108,1
	10000		123,6

TABLE 1: Acquisition Parameters Overview:
For all b-value scans: TR (repetition time) is 10000; half-scan (reducing EPI readout time by filling only a part of k-space) is 0.805; SENSE (sensitivity encoding) is 1, which means no SENSE acceleration. Gradient direction is IS (inferior-superior), matrix size is 112x112, and the voxel size is 2 mm.

B. Data Acquisition

Diffusion MRI scans were acquired on a 7T Achieva system (Philips, Netherlands). The data collected consists of in vivo human brain images of one healthy individual. Two acquisitions were performed, one using the gradient insert (ultra-strong gradient head insert) coil and another without this auxiliary coil (whole-body gradient). The first set was obtained using a maximum gradient amplitude strength of 200 mT/m and a slew rate of 900 T/m/s. The second set was obtained using a maximum amplitude strength of 40 mT/m and 200 T/m/s slew rate. Additionally, dynamic field camera scans were acquired for both situations. The need for additional field scans is to correct for eddy currents distortions, which is explained in subsection C.1. The corresponding acquisition parameters are presented in Table 1.

The gradient insert is a plug and play lightweight coil (45 kg). Two people place the coil on the bed, and it gets positioned in the bore of the 7T scanner by automatically moving the bed before the acquisition. This coil is a single-axis (z-axis) gradient coil; therefore, the diffusion gradients were played along the z-direction [11].

A PGSE sequence with EPI readout was applied for all scans. For RF transmission, the birdcage coil integrated into the gradient insert is used, and for receiving, a 32-channel head coil (Nova Medical, USA) is used [11]. For the whole-body gradient scans, a different RF transmission coil was used. This resulted in a reduction of B1 inhomogeneities artifacts in whole-body scans.

C. Preprocessing pipeline

1) Field camera correction for linear eddy-current-induced distortions: In electromagnetism, the Faraday-Lenz Law explains that electrical currents are created in conductors in proximity to a changing magnetic field. In MRI, rapidly changing magnetic fields through gradient coils or RF coils generate eddy currents in any metallic parts of the scanner, as well as in wires or the patient themselves. These eddy currents can have negative effects on both the scanner and image

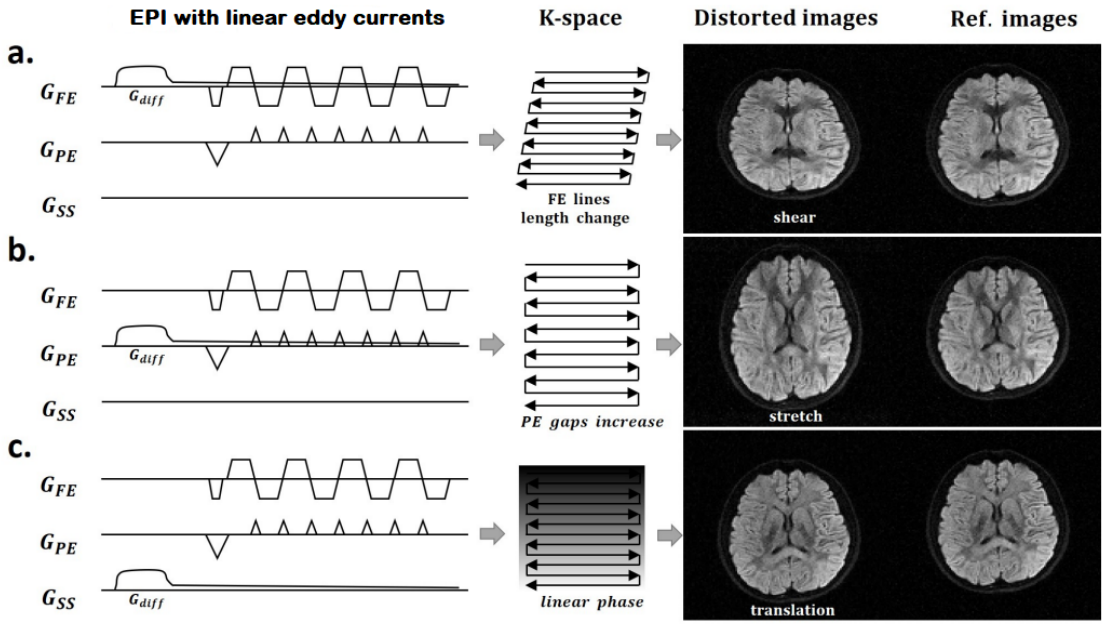


Fig. 4: a) distorted waveform with eddy currents in the frequency encoding direction. Lines are shifted in k-space, and the output is a sheared distorted image, b) eddy currents in the phase encoding direction, increasing space between k-space lines, and results in a stretched(scaled) distorted image, c) eddy currents in the slice selection direction produce a linear phase shift in the phase-encode direction, which subsequently results in a translation artifact in the final image. Adapted from [17].

quality [18]. They create undesired magnetic fields that alter the magnetic field created by the source and produce time-dependent gradients, which can lead to image distortion like Nyquist ghosts or geometric distortions. The intensity of these artifacts is directly proportional to the magnetic field change rate [17]. Additionally, rapid changes in magnetic fields can stimulate the peripheral nerves in the patient [18]. The focus of this work is correcting eddy currents induced in the scanner itself.

In all types of echo-planar imaging (EPI), eddy currents generate geometric distortions such as image shearing in the frequency-encoding direction, image scaling from gradients in the phase-encoding direction, and global position shift (translations) from changes in the main magnetic field (B0) [18]. B0 eddy currents are slight variations in the main magnetic field. These fluctuations are constant in space but vary in time. When strong diffusion gradients are activated and deactivated, eddy currents geometrical distortions are created, resulting in a deviation of the transversed k-space trajectory from the imposed one. This affects the readout gradients in the frequency-encode (x), phase-encode (y), and slice-select (z) directions [17]. As a result, DW-EPI images exhibit visual deformations as shown in Figure 4 above. Furthermore, in DW imaging, these currents can also result in incorrect higher ADC values [18]. This work focuses on correcting first-order (linear) eddy-currents, with the potential for higher-order correction presented in the Discussion section.

One current approach to correct for eddy currents is using FSL Eddy [19], which requires additional reversed phase encoding data acquisition. FSL Eddy requires a minimum of 10 to 15 gradient directions for lower b-values and increases to 30 to 40 for higher b-value scans. This constraint increases the acquisition time for DW imaging as more scans in different directions are needed. FSL Eddy uses affine transformation to align images acquired at different gradient directions and can also perform slice-to-volume motion correction [20]. However, using FSL Eddy with this one-axis gradient insert coil is not practical as the number of gradient directions is limited to one. Therefore, field camera correction seems like a better solution to achieve eddy currents correction while maintaining a short acquisition time.

Field cameras are becoming increasingly popular in research as a solution for correcting eddy current distortions in dMRI data. This is because field cameras can monitor how the magnetic field changes during the EPI readout, and then use this information to correct distortions during image reconstruction [12].

In this work, a dynamic field camera (see Figure 5) consisting of 16 NMR probes was used to measure the evolution of the magnetic field during the EPI readout. A separate session was conducted for the measurement using the same acquisition protocol as for the human scans. The camera was placed at



Fig. 5: Dynamic field camera manufactured by Skope (Zurich) [21].

the isocenter of the gradient insert coil for the measurement. This provided gradient fields and k-space trajectories [21]. The output was generated as raw complex data, which was then retrospectively used as input for a reconstruction MATLAB script. The reconstruction procedure is outlined in the Appendix section of this work, which includes some general steps involved in the process.

2) Susceptibility distortion correction: Since EPI readout is used in this pulse sequence, it is well-known that this technique is susceptible to B0 magnetic field inhomogeneities caused by variations in the magnetic susceptibility of the tissues within the body [12]. These inhomogeneities cause pixels in the image to appear shifted from their expected location [22]. This leads to image artifacts, sometimes referred to as stretching or pile up [23], which can negatively impact the interpretability of the acquired image scans. To mitigate this issue, FSL topup is used to enhance the overall image quality.

In order to use FSL topup, $b = 0\ s/mm^2$ value scans were acquired with reversed phase-encode blips (Right-Left, Left-Right), resulting in the creation of image pairs with distortions in opposite directions. From the pairs of images, a susceptibility-induced fieldmap is estimated. Subsequently, FSL topup employs this estimated fieldmap in conjunction with a similarity measure to determine any displacement that occurred between two acquisitions [24][25]. This fieldmap is furthermore used to correct the other dMRI volumes in a dataset, as susceptibility distortions have an identical effect on all b-value scans in the absence of motion [12] [26]. Additional information regarding the parameters utilized for the FSL topup correction can be found in the Appendix section of this document.

3) B-matrix correction: To prevent nerve stimulation caused by rapidly changing magnetic fields, the gradient insert coil was limited to a field of view of 192 mm [11]. This causes a spatial nonuniformity, which becomes more pronounced as one moves away from the center of the image (isocenter). The drawback of this limitation is that the linearity of the gradient coil is compromised [12]. Consequently, the readout gradients and diffusion encoding are impacted by variations from their intended values, resulting in inconsistencies in the resulting images. These variations in the expected gradients lead to geometric distortions and signal intensity deviations in the resultant images. This is due to the fact that conventional image reconstruction techniques presuppose that the data has been spatially encoded using calibrated linear gradients. As a result, such distortions can pose a significant challenge for preoperative planning or volumetric studies [12].

The preprocessing pipeline presented in this work focuses on correcting gradient deviations. To quantify the spatial variations in the image caused by gradient deviations, a unique B-matrix is assigned to each individual voxel. However, correcting for gradient deviations can be challenging if the specific magnetic fields of the coil are not known. While MRI scanner manufacturers typically have the necessary information for correction, this information is often not readily available to users as it is considered sensitive and proprietary information [12].

It is essential to correct for B-matrix deviations, as they not only affect high DW measurements but also lower-to-moderate DW signals. The latter is because the absolute signal change is larger at these b-values, making them more susceptible to these deviations, as noted in the study by Guo et al. (2020) [27].

The method outlined in the study of Bammer et al. (2003) [28] was applied to correct for the effects of gradient deviations. Laplace's equation states that when a gradient coil is enabled to create a magnetic field in one direction, it also generates magnetic fields in two other directions. This means that the magnetic field produced by the gradient insert coil is different in magnitude and direction from the intended magnetic field.

By knowing the deviations from the desired magnetic field, a gradient coil tensor $L(r)$ can be defined to relate the effective magnetic field produced by the coil at each location r with respect to the desired gradient field. This tensor contains space-varying error terms for each gradient axes (x,y,z). According to Bammer [28], the dependency between the actual gradient insert, $Ginsert_{act}(r)$, and the desired gradient, G, is therefore written as:

$$Ginsert_{act}(r) = \begin{pmatrix} L_{xx} & L_{xy} & L_{xz} \\ L_{yx} & L_{yy} & L_{yz} \\ L_{zx} & L_{xy} & L_{zz} \end{pmatrix} G = L(r)G \qquad (4)$$

The L_{ij} matrix element shows how much of the i-direction magnetic field gradient is produced when a unit gradient in the j-direction is intended. It's calculated by taking the derivative of the effective magnetic field that changes based on location and dividing it by the nominal gradient strength (G_i).

$$L_{ij} = \left(\frac{\partial B_j^i(r)}{\partial j} \right) / G_i, \quad ij = x, y, z \qquad (5)$$

Given the gradient nonuniformity information about the gradient insert coil is known at every point in the defined scanning volume, the effective B-matrix (B_{eff}) can be calculated for each voxel:

$$B_{eff}(r) = L(r) b L(r)^T, \quad b = \text{assumed b-value} \qquad (6)$$

After the effective B-matrix for all pixel values is obtained, the matrix trace will yield the final b value for that specific location.

Once the b-value for each pixel is correctly calculated, the ADC and T2 image is computed using Equation 1. This computation was performed using images with $b = 0, 500, 1000, 3000\ s/mm^2$. This is implemented through a second MATLAB script, and the step-by-step procedure of this algorithm is presented in the Appendix section.

D. Inversion-Recovery pulse sequence simulations

The illustration in Figure 6 on the following page depicts different water pools commonly modelled in dMRI studies. The biophysical model used involves multiple compartments that can identify pathologies such as demyelination or dysmyelination. The compartments include intra-axonal (represented in blue), extra-axonal (represented in green) and myelin

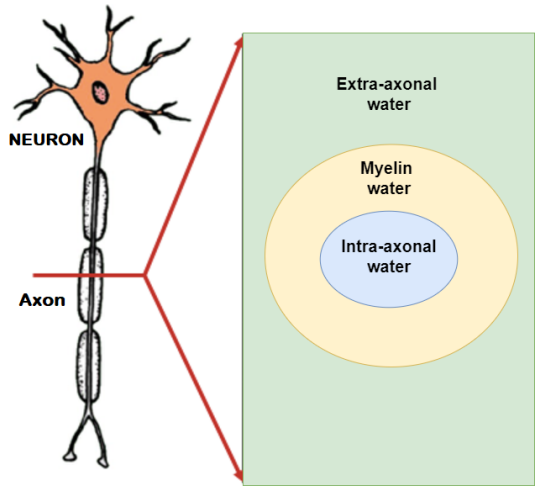


Fig. 6: Cross-section through axon for biophysical modelling in white matter. Adapted from [29].

water (yellow) areas with different parallel and perpendicular diffusion. In general, myelin water is not considered a distinct compartment as its T2 signal is too long to be detected using a standard PGSE pulse sequence (see Figure 1).

The data from this study (as shown in Figure 11) reveals that using ultra-strong gradient inserts can result in shorter echo times (TE) at high b-values if the insert can be used for diffusion encoding.

The hypothesis in Figure 7 suggests an inverse-recovery (IR) pulse sequence to model myelin water independently from the other components.

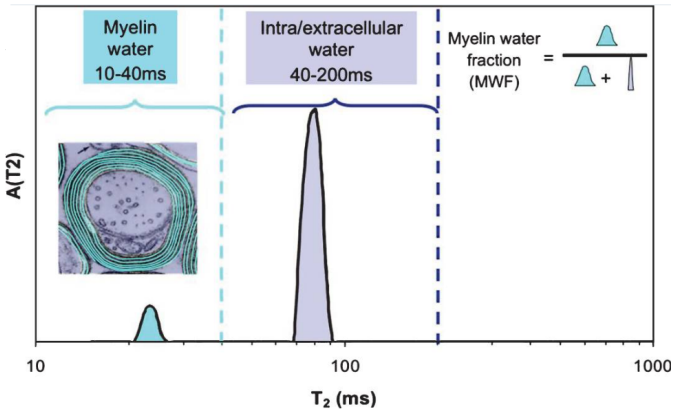


Fig. 7: T2 signal of in vivo human brain from myelin, Intra/extracellular(Intra/extra axonal) water and the corresponding myelin water fraction. Adapted from [30].

The equation of IR pulse sequence [31] is given by:

$$S = k[H](1 - 2e^{-TI/T1} + e^{-TR/T1})e^{-TE/T2}, \tag{7}$$

with K as a scaling factor, H is the spin density, TI is the inversion time, TR is the repetition time, TE is the echo time, $T2$ is the transverse relaxation time and $T1$ is the longitudinal relaxation time. In this equation, by selecting the right TI, it is possible to eliminate non-myelin water pools with a specific $T1$. Thus, an Inverse-Recovery sequence (as shown in Figure 8) can be used to eliminate the long $T1$ component in white matter (WM), which is commonly thought to come from non-myelin water (as mentioned in [30]). The myelin water fraction (MWF) is a biomarker in the study of neurodegenerative diseases, and it is typically defined as the proportion of the $T2$ distribution originating from myelin water (10 to 40 ms) to the total $T2$ distribution. When suppression is accomplished, the myelin water fraction can be represented by just one diffusion-T2 compartment, thereby simplifying the fitting procedure.

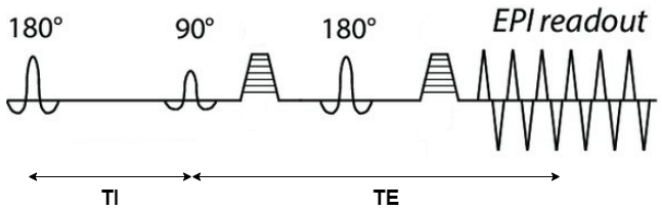


Fig. 8: Inversion-DW-EPI pulse sequence. TI is the inversion time, TE is the echo time. Adapted from [32].

For the simulation, the signal model to fit is:

$$S = S_0 e^{-bg^T Dg} e^{-TE/T2}, \tag{8}$$

with S_0 the measured signal without a diffusion-sensitizing gradient, S is the signal which depends on gradient directions, b describes the pulse sequence, gradient strength (see equation 2) [33]. The dependence on TE and $T2$ is modelled as well.

The protocol set up for the simulations uses minimum echo times from figure 11 to investigate gradient settings (see Table 3 below).

gradient insert			
b values [ms/µm^2]	min TE [ms]	max TE [ms]	measurements
b = 0	21.83	100	7
b = 1	31.57	100	7
b = 2	36	100	7
b = 3	37.73	100	7
whole-body gradient			
b values [ms/µm^2]	min TE [ms]	max TE [ms]	measurements
b = 0	36.98	100	7
b = 1	71.17	100	7
b = 2	80	100	7
b = 3	90.98	100	7

TABLE 3: Table showing simulation settings for gradient insert and whole-body gradient

For both scenarios, three gradient directions were considered: [1,0,0]; [0,1,0] and [0,0,1]. Ground truth values for S_0, $d_\parallel$ (parallel diffusivity), $d_\perp$ (perpendicular diffusivity), and $T2$ were set to: 1, 0.37 $\mu m^2/ms$, 0.13 $\mu m^2/ms$ and 14 ms. $T2$ was arbitrarily chosen to be 14 ms, within the range of 10 to 40 ms (see figure 7).

The values for $d_\parallel$ and $d_\perp$ are taken from Andrews et. al., 2006 [35]. In their experiment, the mean ADC of myelin water in an excised sciatic nerve from a frog was computed.

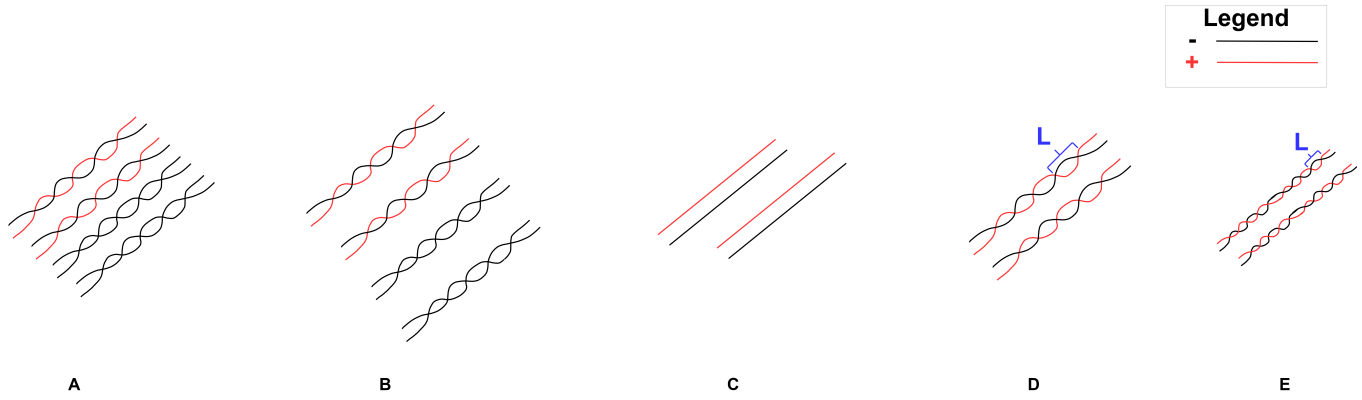


Fig. 9: Cables Arrangements: A) starting setup with four twisted pairs (a pair = two current-carrying cables), B) creating a distance between the pairs, C) functional pairs are separated and untwisted, D) functional pairs are twisted again with a half twist of length L, E) pairs are twisted better with a smaller length for the half twists.

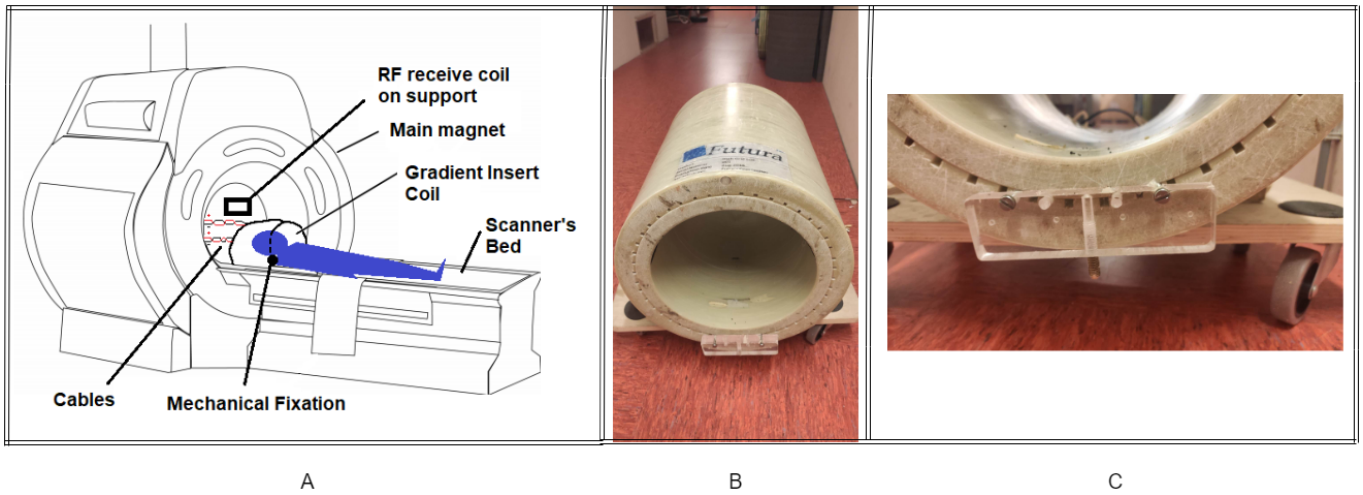


Fig. 10: A) Image overview for scanning with a gradient insert coil. Cables' configuration included. Adapted from [34], B) Image with the gradient insert coil, C) Image zoomed on the mechanical fixation.

The fitting was done using $lsqnonlin$ function in MATLAB [36]. The initial guess parameters were set to: 1, 1 $\mu m^2/ms$, 1 $\mu m^2/ms$ and 20 ms, based on the ground truth values previously mentioned. In the simulation, Gaussian-distributed noise with a standard deviation of 0.01 (SNR equal to 100) was added to signal S (equation 7). This process was repeated 500 times to account for multiple noise iterations.

III. Results

A. Experimental Setup with the cables

To acquire DW images, the starting setup had to be modified to limit the magnetic force that move the cables considerably. Different cable arrangements have been tested to maintain the connector's integrity, as shown in Figure 9 above.

The default configuration had four pairs (Figure 9, A). Each pair has two current-carrying cables, and in Figure 9, it is represented by one red and one black line. The colours represent the direction of the moving charges (the direction of the current) through the cables. The first two configurations contained two redundant cable pairs not used to supply power to the coil (illustrated by black twisted pairs in Figure 9 A and B). Therefore, they were removed in the third arrangement (C) for efficiency. In the second arrangement (B), the distance between the pairs was increased, but there was no change in the magnitude of the magnetic force, which showed forceful cables movement. The third arrangement aimed to test when the functional pairs were not twisted but isolated with black tape. The outcome was not positive. The motion of the cables was powerful enough to make DW scans at low b-values impossible.

The cables were twisted again with the fourth configuration (D), but the structure was unstable enough for low currents such as 200 or 300 Ampers. Finally, the solution (E) was to make the length L of the half twists smaller. For this operation, two people are needed at the ends of two cables to stretch after every roll, making the half twists more compact. Additionally, the cables were tied together to keep them stationary at high currents. Cables have opposite polarities in neighbouring half twists, and this causes the net magnetic field (Figure 3) between them to cancel out [16]. The conclusion is that increasing the distance between the cables produces a greater

local magnetic field and an inconvenient angle θ between the current i and $\vec{B}$. Twisting cables allows DW imaging since it helps align the cables parallel with the direction of $\vec{B}$ and reduces the electromagnetic interference between cables. Otherwise, the connector can break at a mighty move. However, the magnetic force is not eliminated since the best angle θ is hard to obtain due to mechanical limitations inside the bore. Still, the magnetic force is limited enough to enable a limited number of DW acquisitions using this gradient insert coil. Possible improvements are presented in the Discussion section.

The cable movement also impacted the gradient insert coil itself to shift slightly during scanning as the cable pulled on the coil. Therefore, a mechanical support was created to keep the coil fixed to the bed. Moreover, the RF receive coil of the main magnet had to be placed on an improvised support to protect it from pressing the cables (see Figure 10 on the previous page).

B. Data Acquisition

The benefits of using a gradient insert coil compared to a whole-body gradient are shown graphically in Figure 11. The echo times of the gradient insert scans are lower for the same b-value scans, leading to a reduction in scanning time and improved comfort for patients.

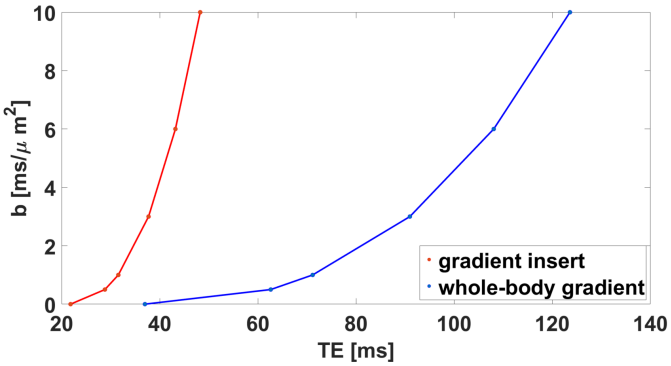


Fig. 11: DW Acquisitions.

C. Preprocessing pipeline

1) Field camera correction for linear eddy-current-induced distortions: Figure 12 shows multiple DW scans obtained for the same slice at varying b-values for gradient insert data. The $b = 0\ s/mm^2$ image is not affected by eddy currents, and it is used as the reference. The edges of the $b = 0\ s/mm^2$ are superimposed onto other DW images [37], resulting in spatial deviations where the edge mask does not fully overlap with the expected pixel information. The output shown in Figure 13 reveals that the MATLAB 1 (see Appendix) post-processing script successfully corrected the geometric deformations created by the linear eddy-currents. In Figure 14, the same quality control is applied to the whole-body data. However, unlike before, we have fewer eddy current effects because the gradient amplitude strength is lower.

Figures 16 and 17 show how the dynamic field camera measures gradient fields and k-space trajectories. A shear deformation can be identified for the gradient insert gradient when looking at the k-space measured trajectories. In contrast, the k-space measurement for the whole-body image data almost matches the ideal case.

2) Susceptibility distortion correction: Figures 18 and 19 show the correction of the $b = 0\ s/mm^2$ image and the estimated field map for the gradient insert and whole-body gradient data scans, respectively. It can be concluded that FSL Topup effectively reduces distortions.

3) B-matrix correction: The findings depicted in Figure 20 demonstrate the largest corrections at the edges of the brain and in the lateral ventricles. The B-matrix correction is applied only to the gradient insert images because of the nonlinearity of the gradient coil. For comparison, ADC has been calculated for the whole-body images in Figure 21. When comparing the ADC values obtained from gradient insert scans, higher values of ADC are spotted in the whole-body images for the selected region of interest. The mean absolute value of corrected ADC for gradient insert is 0.7472 $\mu m^2/ms$, which is lower than 0.9647 $\mu m^2/ms$ for the whole-body.

D. Inversion-Recovery pulse sequence simulations

The data presented in Figures 22 and 23 show that using whole-body settings for acquisition is not a viable option. The values for parallel and perpendicular diffusivities are too far from the reference values. Additionally, the T2 values for the whole-body approach are estimated at higher values than the maximum expected (40 ms, see Figure 7).

On the other hand, the gradient insert approach provides much closer estimates to the ground truth values for diffusivity metrics, as well as modelling T2 signal in the desired range (10 to 40 ms). To facilitate a clearer comparison, the Root Mean Squared Error (RMSE) was calculated and presented in Table 2. The results demonstrate that simulation errors are significantly higher when using the whole-body gradient settings as opposed to the gradient insert settings.

In Figure 24, the SNR was varied in increments of 10 for the gradient insert settings in order to study the effect of different noise distributions on the model. The exponential trend indicates that as the SNR improves, the predicted errors decrease.

RMSE	gradient insert	whole-body gradient
S0	0.4095	0.7817
d∥	0.0651	0.3352
d⊥	0.0338	0.1281
T2	8.008	24.380

TABLE 2: RMS metric comparison between gradient insert and whole-body diffusion properties.

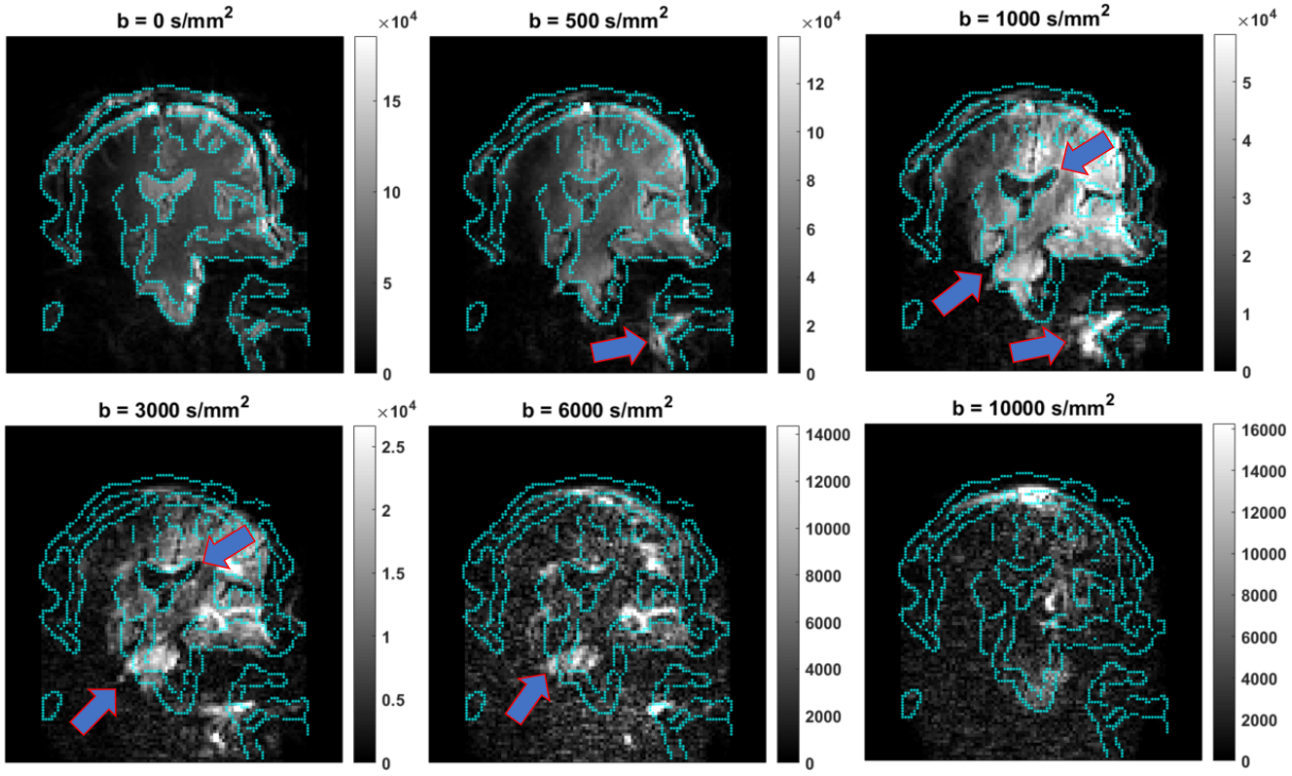


Fig. 12: Gradient insert images before eddy-current correction. Edges of $b = 0\ s/mm^2$ head image are superimposed onto other b-value scans images with a cyan colour [37]. Blue arrows indicate deviations with respect to the $b = 0\ s/mm^2$ reference image.

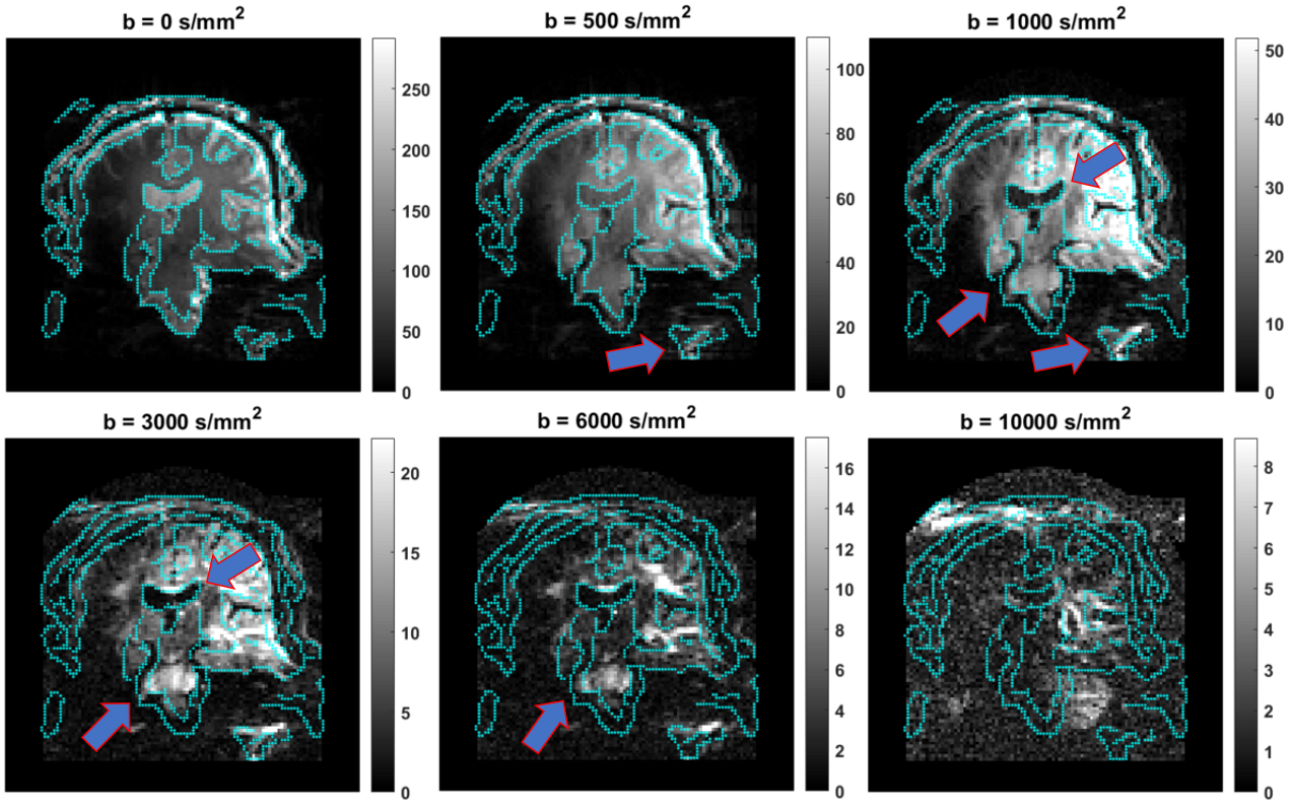


Fig. 13: Gradient insert images after eddy-current correction with a field camera. Edges of $b = 0\ s/mm^2$ head image are superimposed onto other b-value scans images with a cyan colour [37]. Blue arrows indicate no deviation with respect to the $b = 0\ s/mm^2$ reference image.

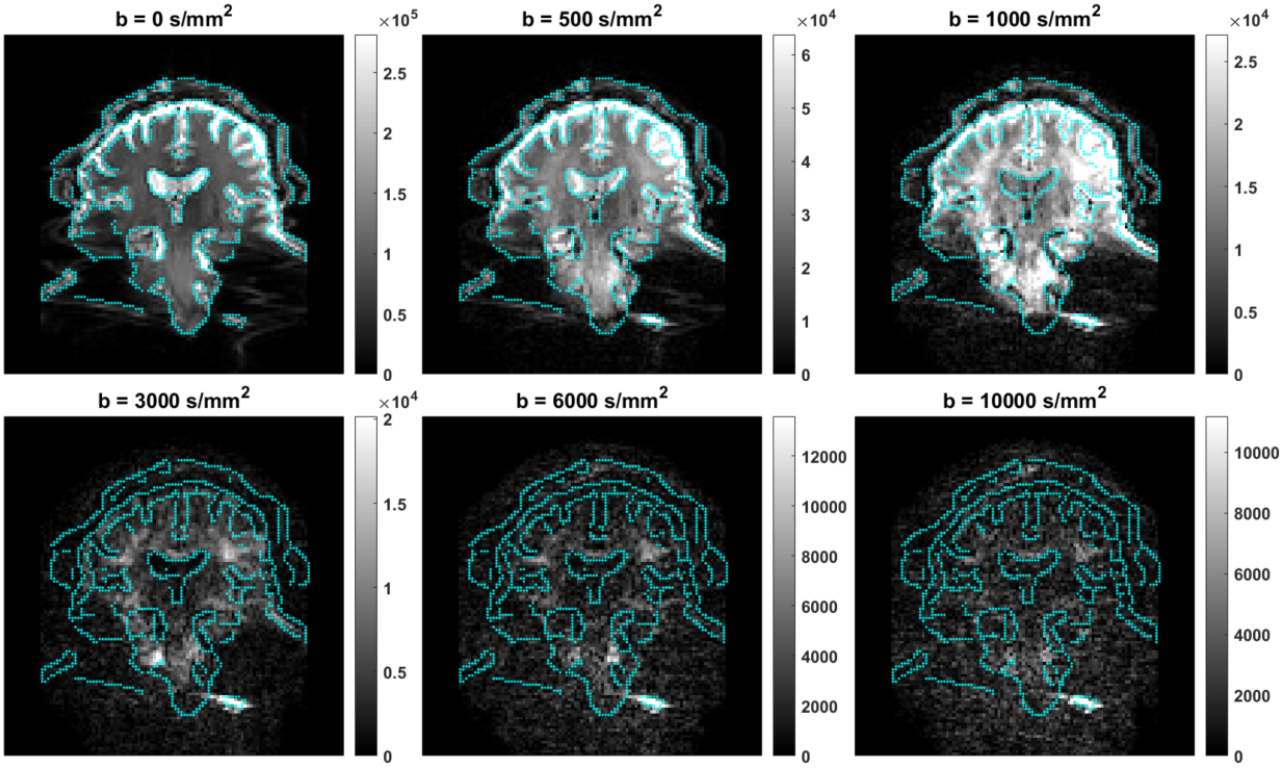


Fig. 14: Whole-body images before eddy-current correction. Edges of $b = 0\ s/mm^2$ head image are superimposed onto other b-value scans images with a cyan colour [37].

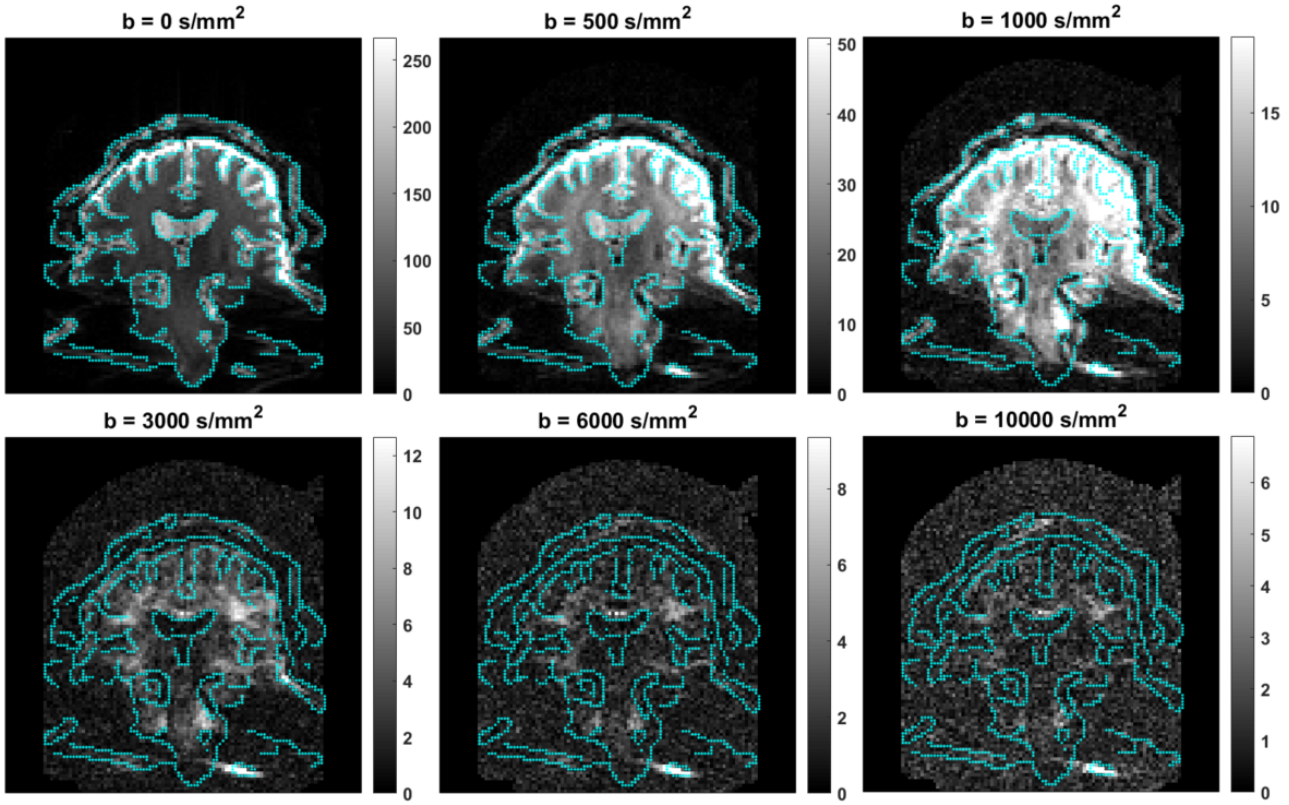


Fig. 15: Whole-body images after eddy-current correction. Edges of $b = 0\ s/mm^2$ head image are superimposed onto other b-value scans images with a cyan colour [37].

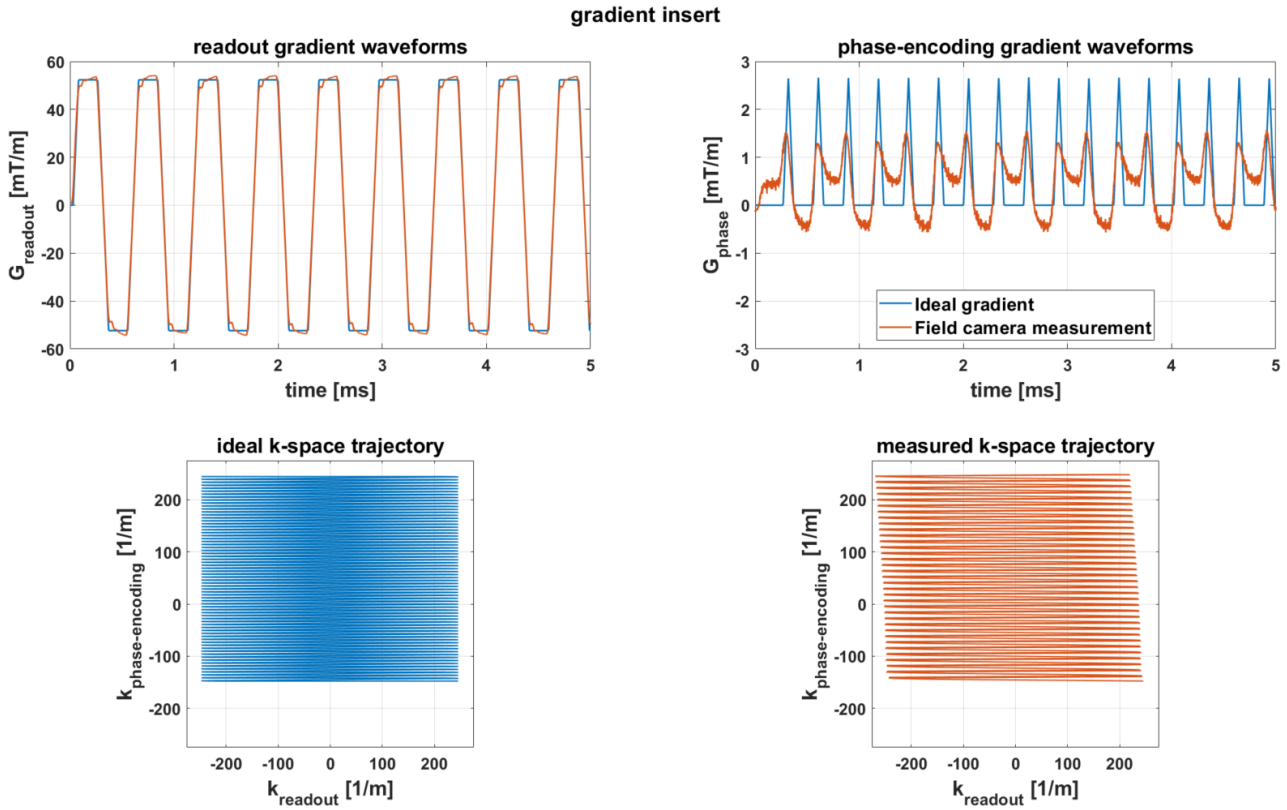


Fig. 16: Top row: Gradient insert waveforms. Bottom row: Ideal k-space trajectories in contrast to measured K-space trajectories.

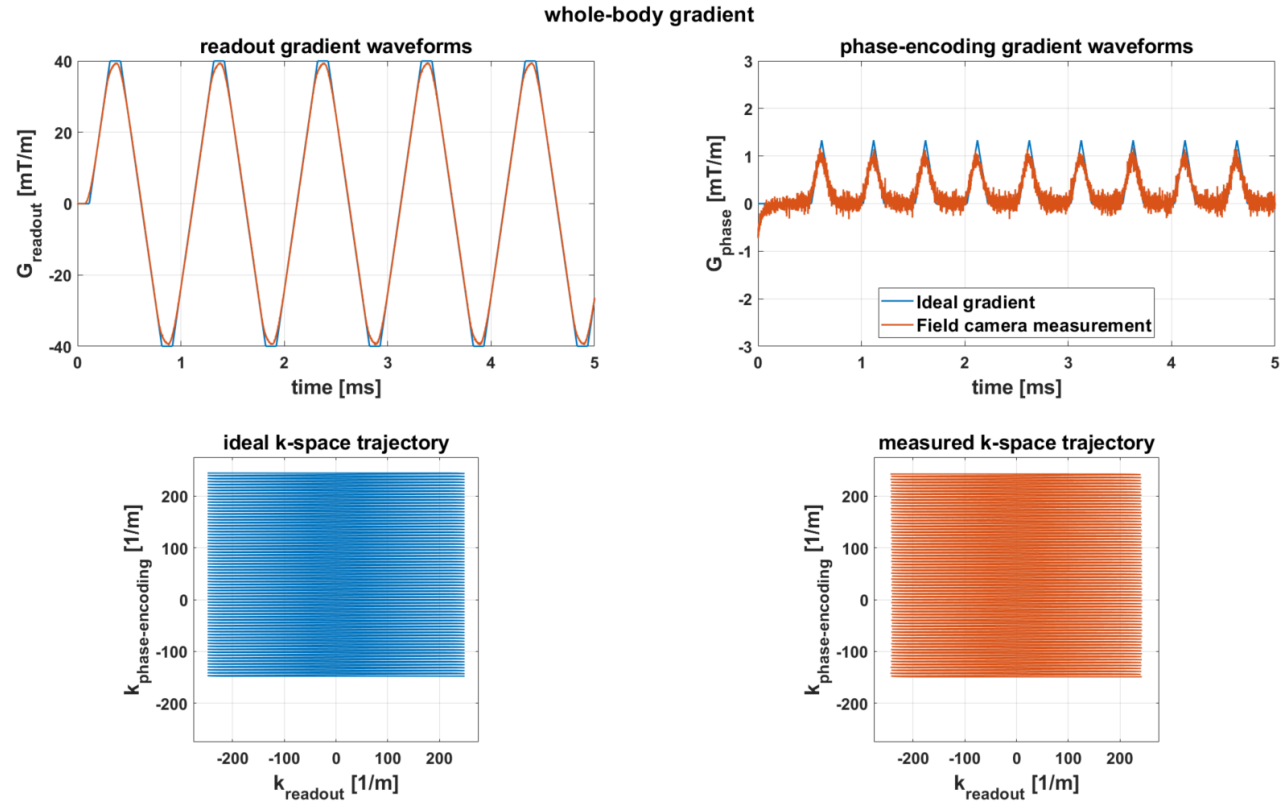


Fig. 17: Top row: Whole-body gradient waveforms. Bottom row: Ideal k-space trajectories in contrast to measured K-space trajectories.

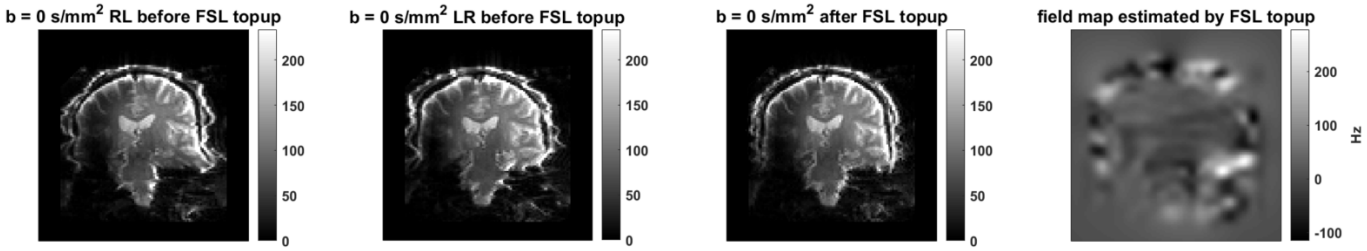


Fig. 18: Susceptibility distortion correction for gradient insert $b = 0\ s/mm^2$ image with FSL topup. The last image shows the field map estimated by FSL topup, with each pixel representing the value of the off-resonance field, expressed in units Hz.

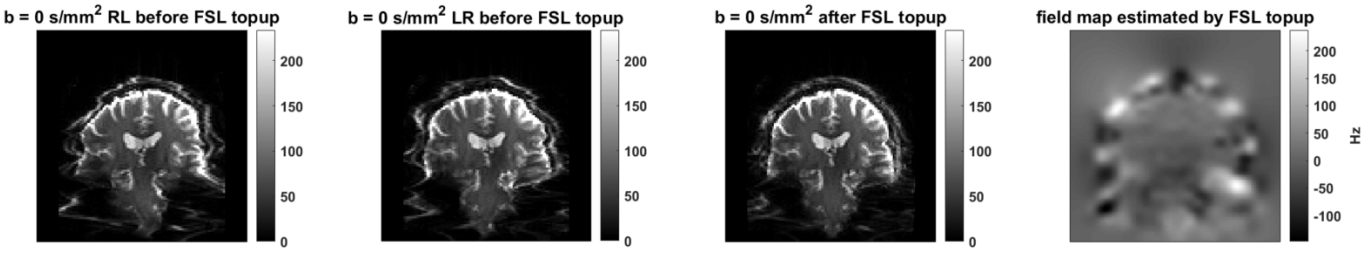


Fig. 19: Susceptibility distortion correction for whole-body $b = 0\ s/mm^2$ image with FSL topup. The last image shows the field map estimated by FSL topup, with each pixel representing the value of the off-resonance field, expressed in units Hz.

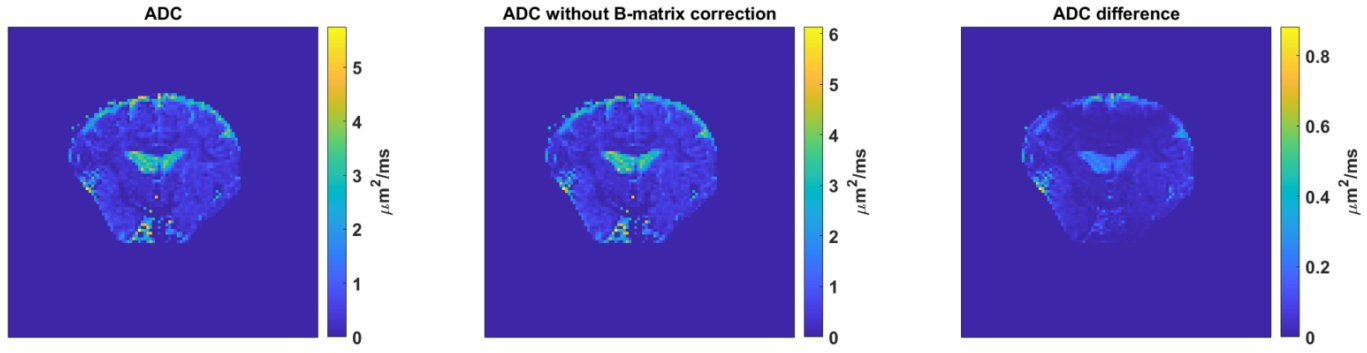


Fig. 20: ADC with and without B-matrix Correction for the gradient insert images; $b = 0, 500, 1000, 3000\ s/mm^2$ images were used to obtain this result. The upper limit of the scale is set to the maximum pixel value.

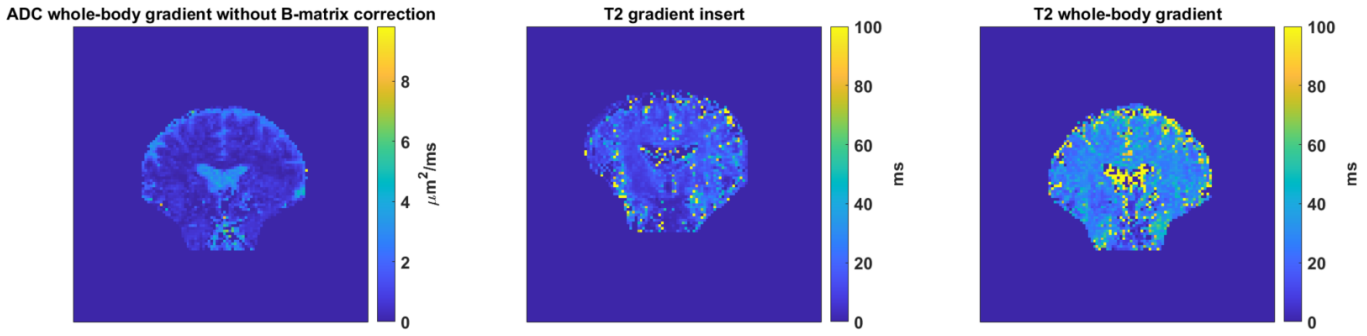


Fig. 21: ADC without B-matrix correction for the whole-body gradient images. The upper limit of the scale is set to the maximum pixel value. The last two images show the estimated T2 image of gradient insert and whole-body gradient images; $b = 0, 500, 1000, 3000\ s/mm^2$ images were used to obtain this result. The scale for the last two images is set to 0-100 ms.

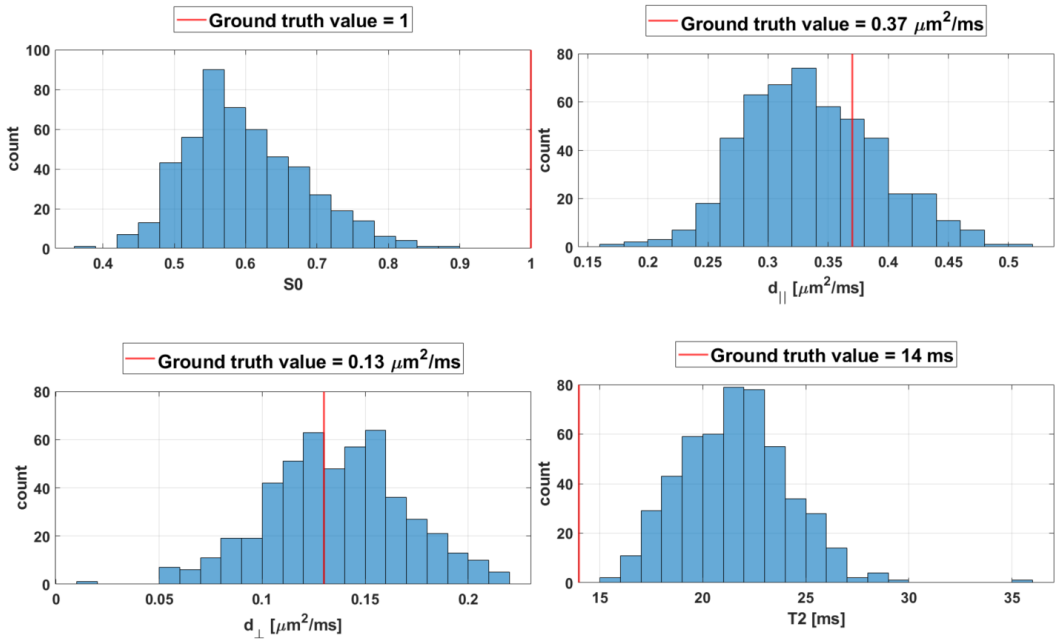


Fig. 22: Simulation of diffusion parameters and ground truth values for gradient insert settings.

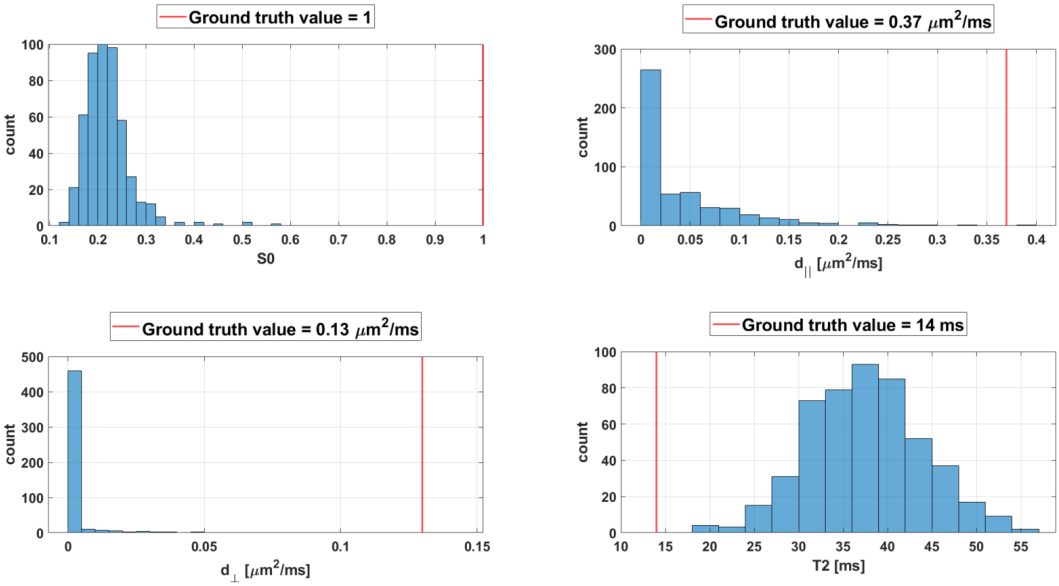


Fig. 23: Simulation of diffusion parameters and ground truth values for whole-body settings.

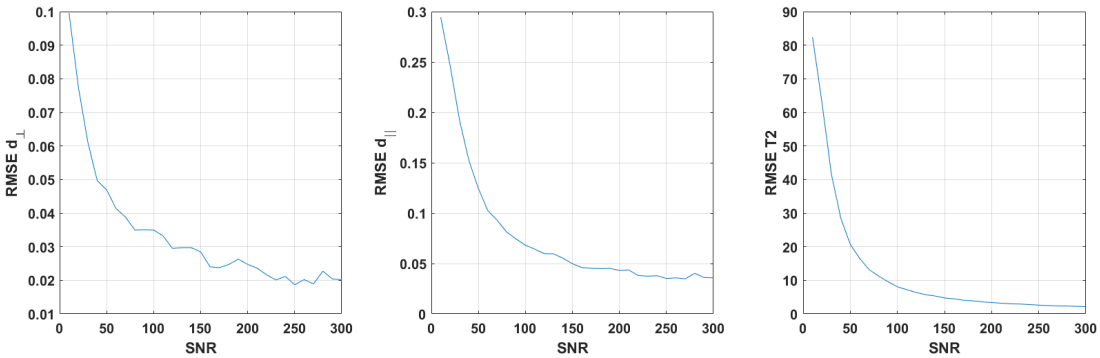


Fig. 24: Simulation of RMSE for $d_{\|}$, $d_{\perp}$ and T2 for different SNR values.

IV. Discussion

A. Experimental Setup with the cables

In this harness, pairs are not shielded. The usage of coaxial straight cables can drastically reduce the electromagnetic interference between the pairs [38]. This is because shielded cables have positive and negative conductors in the same wire [39]. More important, the magnitude of the magnetic force can be reduced more if the direction of the moving charges is closely aligned with the magnetic field produced by the main magnet [13][14]. Figure 25 illustrates a proposal where a rigid support could be attached to the gradient insert coil before the scan starts.

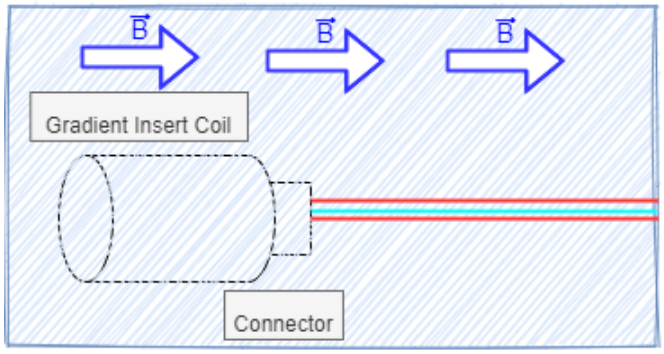


Fig. 25: The sketched light blue rectangle depicts the bore of the 7T scanner. $\vec{B}$ is the magnetic field created by the main magnet. The cyan line represents a single coaxial cable used to supply power to the gradient insert coil. The red lines depict a rigid support designed to hold the cable in a parallel alignment with respect to the main magnetic field.

The results of these experiments predict the need for further investigation to determine the optimal configuration for making this gradient insert coil prototype suitable for longer diffusion-weighted acquisitions at high b-values.

B. Data Acquisition

In the acquisition process, only 20 slices were obtained using the gradient insert coil due to magnetic force limitation. These cables still moved for scans at the values of $b = 6000, 10000 s/mm^2$. To overcome this limitation, improving the cable setup and verifying the magnitude of the force before retesting with more slices is crucial.

The estimation of T2 yields inaccurate values for the given protocols, hence, the computation of T2 for both datasets is not possible. To accurately estimate different echo times with varying b values, it is necessary to use protocols incorporating more b value scans with longer TE. Therefore, acquiring a $b = 0\ s/mm^2$ scan for each echo time is crucial for obtaining accurate T2 values.

C. Preprocessing pipeline

In this work, EPI readout was used. With spiral readout, echo times can be reduced, leading to a boost in image SNR. Spiral MRI differs from EPI in that it cannot use EPI-phase correction techniques to account for encoding perturbations caused by short-term eddy currents. Therefore, in this scenario, the ability of dynamic field monitoring to deliver accurate encoding information is of great significance [21]. Static B0 off-resonance is another factor that can result in blurring in spiral MRI due to encoding inaccuracies. This static off-resonance is usually determined through multi-echo gradient sequences. Dynamic field monitoring can improve the accuracy of field mapping during imaging studies by capturing slow dynamic field changes that occur during the scanning process, even though it cannot directly measure static off-resonance in the subject. Obtaining precise measurements of both dynamic and static encoding fields leads to high-quality DW images with improved SNR in comparison to EPI [40][41][42].

This work employs field camera correction to address linear eddy currents, and it has the capability to be extended to correct for higher order eddy currents as well [43].

The correction of susceptibility-induced distortions relies on the assumption that the susceptibility field remains constant throughout the acquisition process. As a result, either the same deformation field or its rotated version (depending on motion) is applied to all DW images. However, this method neglects the relationship between the susceptibility fields and head orientation and thus ignores the effect of subject motion. A new method for estimating susceptibility fields per volume was recently introduced by Andersson et al., 2018a [44]. This technique adjusts the estimated fieldmap based on the impact of subject motion on the susceptibility-induced distortions, as movement can change the spatial location and strength of the field. This approach has demonstrated improved anatomical accuracy of computed diffusion metrics and increased data reproducibility, especially in situations where the subject experiences significant movement, such as when scanning patients or children [12].

B-matrix correction is usually performed towards the end of a preprocessing sequence, after the correction of subject motion or eddy currents. However, if the subject underwent any movement, the L(r) matrix (as per equation 4) corresponding to their original position in the scanner must be considered. Therefore, the B-matrix can change both spatially and temporally. Rudrapatna et al. (2021) have devised a method for computing B-matrices that takes into account both spatial and temporal variations [45]. They use estimated motion parameters to trace the temporal changes in gradient amplitudes for each location, resulting in a spatiotemporal B-matrix. Their findings indicate that the spatiotemporal B-matrix approach could result in more reliable parameter estimations in circumstances of high gradient nonlinearities and excessive movement [12].

The results of the B-matrix correction show that the mean ADC value obtained using the whole-body gradient is higher compared to the one obtained using the gradient insert acquisition. This difference is expected, as the amplitude strength of the whole-body gradient is lower. This may suggest the presence of T2 signals from multiple tissues. Nonetheless, using ultra-strong gradient coils leads to shorter ADC values, but it provides valuable T2 information, particularly important in the context of modelling myelin water tissue.

D. Inversion-Recovery pulse sequence

In this study, an IR pulse was proposed to model the diffusion characteristics of myelin water. The research conducted by Andrews et al. utilized a Double-Inversion-Recovery (DIR) protocol in combination with PGSE to determine the ADC of myelin water [35]. IR sequences can be used to null the signal of one tissue by choosing TI. In a practical application, a more thorough signal suppression may be required. The implementation of a double inversion recovery (DIR) sequence can help achieve this goal by suppressing signals of two tissues (can be from both grey and white matter tissues) [46].

V. Conclusion

In conclusion, this work presented a preprocessing pipeline for dMRI images that were obtained with and without an ultra-strong gradient insert. To resolve the technical challenges associated with cable arrangement, a solution was offered. Additionally, a simulation of diffusion parameters that took into account an inverse-pulse sequence was carried out. The simulation showed the capability to model myelin water T2 at short TE with an ultra-strong gradient insert coil, highlighting the usefulness of the IR pulse sequence. The presented work makes a step forward in the examination of demyelination and dysmyelination through improved image quality. This improvement opens up the potential for strong diffusion MRI to become a diagnostic tool for Alzheimer's disease [47][48][49][50] but also for other neurodegenerative diseases in the future [30].

APPENDIX

Preprocessing Pipeline Steps:

1. Field camera processing. For each set of data (image data and k-space trajectories from the dynamic field camera), the following steps were followed:

MATLAB 1

1: Load complex raw image data
2: Load k-space trajectories derived from field camera data
3: Generate Nonuniform Fast Fourier Transform (NUFFT) using measured k-space trajectory to compensate for eddy currents from gradient-insert.
4: Use NUFFT in Conjugate-gradient SENSE reconstruction to obtain images

Contact Edwin Versteeg for additional information about this script.

2. The second step is to correct the susceptibility-induced distortions using FSL topup. Following the instructions from FSL topup website [26], $b = 0\ s/mm^2$ RL and LR images have to be mixed into one file. Onto this file, the next step is to call "topup" command with parameter "- - estmov=0". Without this setting, the information on the first and last slice is lost, and in this situation, we wanted to make use of all slices. This function applies least-squares restoration for the $b = 0\ s/mm^2$ image, which yield the results shown in Figures 18 and 19. Additionally, it estimates the field map used to correct the other DW images. The correction itself is made by calling "applytopup" command function with the right acquisition parameters set in the text file: 1, 0, 0 TE for the RL image; -1, 0, 0 TE for the LR image. For the other DW images, only RL acquisitions are available, therefore, when running the "applytopup" command, it is necessary to specify the "- - method=jac" option.

3. Step-by-step approach for B-matrix correction and computing ADC and T2 images.

Before applying the correction, the skull is removed from the selected slice by using ROI (region of interest) selection. This method is more efficient and faster than using FSL bet because, with eddy-currents corrected and other DW images aligned with the reference $b = 0s/mm^2$ image, one mask can be effectively applied on all b-value scans on the selected slice. arrShow [51] can be used to generate the positions of the ROI and then are imported in the MATLAB 2 script.

a) B-matrix correction: described in MATLAB 2 pseudocode.

MATLAB 2

1: Load parrec images for getting TE values from DICOM and offcenter positions.
2: Load nifti images corrected by FSL topup
3: Calculate nominal gradient field from linear regions of the gradient insert coil.
4: **for** $offcenter = 1, 2, \ldots$ **do**
5: Compute a grid with coordinates based on the FOV, the voxel size and the offcenters.
6: For the new grid, compute the x,y,z components of the magnetic field.
7: Normalize the magnetic field components with the nominal gradient field.
8: Compute Lij matrix elements for the current offcenter (the current slice) by computing the gradient in x,y,z direction with a 2mm step (depends on voxel size).
9: **end for**
10: Build the L matrix (equation 4), given the Lij matrix elements.
11: Calculate B-matrix for every pixel (using equation 6), for all the b-value scans included in the processing.
12: The final b-value for the specific pixel is the trace of every B-matrix.

b) computing ADC and T2: Using equation 1, compute ADC and T2 images with iterative weighted LS fit (12 iterations), with weight = $pixelvalue^2$ [52].

ACKNOWLEDGEMENT

I want to thank all my supervisors for their support throughout my work. Their guidance and mentorship have been instrumental in my progress. I would also like to express my gratitude to prof. dr. Dennis Klomp for providing the mechanical fixation for the gradient insert coil. Thank you to everyone for their contributions to this research.

REFERENCES

[1] E. Medina, "Demyelinating and Dysmyelinating Diseases," *Rivista di Neuroradiologia*, vol. 6, no. 2_suppl, pp. 33–38, May 1993, publisher: SAGE Publications. [Online]. Available: https://doi.org/10.1177/19714009930060S205
[2] D. Mcrobbie, E. Moore, M. Graves, and M. Prince, "MRI from picture to proton," *MRI from Picture to Proton*, pp. 1–397, Jan. 2006.
[3] "Gradient coils." [Online]. Available: http://mriquestions.com/gradient-coils.html
[4] "Diffusion MRI - an overview | ScienceDirect Topics." [Online]. Available: https://www-sciencedirect-com.proxy.library.uu.nl/topics/neuroscience/diffusion-mri
[5] "Diffusion." [Online]. Available: http://mriquestions.com/what-is-diffusion.html
[6] E. O. Stejskal and J. E. Tanner, "Spin Diffusion Measurements: Spin Echoes in the Presence of a Time-Dependent Field Gradient," *Journal of Chemical Physics*, vol. 42, pp. 288–292, Jan. 1965, aDS Bibcode: 1965JChPh..42..288S. [Online]. Available: https://ui.adsabs.harvard.edu/abs/1965JChPh..42..288S
[7] R. Bammer, "Basic principles of diffusion-weighted imaging," *European Journal of Radiology*, vol. 45, no. 3, pp. 169–184, Mar. 2003. [Online]. Available: https://www.sciencedirect.com/science/article/pii/S0720048X02003030

[8] "To BOLDly Go: fMRI, Perfusion and Diffusion," in *MRI from Picture to Proton*, 3rd ed., D. W. McRobbie, E. A. Moore, M. J. Graves, and M. R. Prince, Eds. Cambridge: Cambridge University Press, 2017, pp. 303–325. [Online]. Available: https://www.cambridge.org/core/books/mri-from-picture-to-proton/to-boldly-go-fmri-perfusion-and-diffusion/8BB6B5BBC4148262D1608C0A624BEDC5

[9] D. K. Jones, D. C. Alexander, R. Bowtell, M. Cercignani, F. Dell'Acqua, D. J. McHugh, K. L. Miller, M. Palombo, G. J. M. Parker, U. S. Rudrapatna, and C. M. W. Tax, "Microstructural imaging of the human brain with a super-scanner: 10 key advantages of ultra-strong gradients for diffusion MRI," *NeuroImage*, vol. 182, pp. 8–38, Nov. 2018. [Online]. Available: https://www.sciencedirect.com/science/article/pii/S1053811918304610

[10] "(ISMRM 2019) Characterizing diffusion of myelin water in the living human brain using ultra-strong gradients and spiral readout." [Online]. Available: https://archive.ismrm.org/2019/1115.html

[11] E. Versteeg, T. A. van der Velden, C. C. van Leeuwen, M. Borgo, E. R. Huijing, A. D. Hendriks, J. Hendrikse, D. W. J. Klomp, and J. C. W. Siero, "A plug-and-play, lightweight, single-axis gradient insert design for increasing spatiotemporal resolution in echo planar imaging-based brain imaging," *NMR in Biomedicine*, vol. 34, no. 6, p. e4499, 2021, _eprint: https://onlinelibrary.wiley.com/doi/pdf/10.1002/nbm.4499. [Online]. Available: https://onlinelibrary.wiley.com/doi/abs/10.1002/nbm.4499

[12] C. M. W. Tax, M. Bastiani, J. Veraart, E. Garyfallidis, and M. Okan Irfanoglu, "What's new and what's next in diffusion MRI preprocessing," *NeuroImage*, vol. 249, p. 118830, Apr. 2022.

[13] S. J. Ling, W. Moebs, and J. Sanny, "11.4 Magnetic Force on a Current-Carrying Conductor," Sep. 2016, book Title: University Physics Volume 2 Publisher: OpenStax. [Online]. Available: https://pressbooks.online.ucf.edu/osuniversityphysics2/chapter/magnetic-force-on-a-current-carrying-conductor/

[14] "Magnetic forces." [Online]. Available: http://hyperphysics.phy-astr.gsu.edu/hbase/magnetic/magfor.html

[15] "Magnetic Force on a Current-Carrying Conductor | Physics." [Online]. Available: https://courses.lumenlearning.com/suny-physics/chapter/22-7-magnetic-force-on-a-current-carrying-conductor/

[16] "How Cable Twisting Improves EMI," Aug. 2016. [Online]. Available: https://emianalyst.wordpress.com/2016/08/31/how-cable-twisting-improves-emi/

[17] X. Liu, "Advanced High Resolution Diffusion Tensor Magnetic Resonance Imaging," Ph.D. dissertation, Dec. 2020.

[18] "Eddy currents." [Online]. Available: http://mriquestions.com/eddy-current-problems.html

[19] J. L. R. Andersson and S. N. Sotiropoulos, "An integrated approach to correction for off-resonance effects and subject movement in diffusion MR imaging," *NeuroImage*, vol. 125, pp. 1063–1078, Jan. 2016. [Online]. Available: https://www.sciencedirect.com/science/article/pii/S1053811915009209

[20] "eddy - FslWiki." [Online]. Available: https://fsl.fmrib.ox.ac.uk/fsl/fslwiki/eddy

[21] "Skope Dynamic Field Camera." [Online]. Available: https://skope.swiss/products/dynamic-field-camera/

[22] P. Jezzard and R. S. Balaban, "Correction for geometric distortion in echo planar images from B0 field variations," *Magnetic Resonance in Medicine*, vol. 34, no. 1, pp. 65–73, 1995, _eprint: https://onlinelibrary.wiley.com/doi/pdf/10.1002/mrm.1910340111. [Online]. Available: https://onlinelibrary.wiley.com/doi/abs/10.1002/mrm.1910340111

[23] M. Usman, L. Kakkar, A. Matakos, A. Kirkham, S. Arridge, and D. Atkinson, "Joint B0 and image estimation integrated with model based reconstruction for field map update and distortion correction in prostate diffusion MRI," *Magnetic Resonance Imaging*, vol. 65, pp. 90–99, Jan. 2020. [Online]. Available: https://www.sciencedirect.com/science/article/pii/S0730725X19300372

[24] S. M. Smith, M. Jenkinson, M. W. Woolrich, C. F. Beckmann, T. E. J. Behrens, H. Johansen-Berg, P. R. Bannister, M. De Luca, I. Drobnjak, D. E. Flitney, R. K. Niazy, J. Saunders, J. Vickers, Y. Zhang, N. De Stefano, J. M. Brady, and P. M. Matthews, "Advances in functional and structural MR image analysis and implementation as FSL," *NeuroImage*, vol. 23 Suppl 1, pp. S208–219, 2004.

[25] J. L. R. Andersson, S. Skare, and J. Ashburner, "How to correct susceptibility distortions in spin-echo echo-planar images: application to diffusion tensor imaging," *NeuroImage*, vol. 20, no. 2, pp. 870–888, Oct. 2003.

[26] "topup - FslWiki." [Online]. Available: https://fsl.fmrib.ox.ac.uk/fsl/fslwiki/topup

[27] "The effect of gradient nonlinearities on fiber orientation estimates from spherical deconvolution of diffusion magnetic resonance imaging data - Guo - 2021 - Human Brain Mapping - Wiley Online Library." [Online]. Available: https://onlinelibrary-wiley-com.proxy.library.uu.nl/doi/full/10.1002/hbm.25228

[28] R. Bammer, M. Markl, A. Barnett, B. Acar, M. Alley, N. Pelc, G. Glover, and M. Moseley, "Analysis and generalized correction of the effect of spatial gradient field distortions in diffusion-weighted imaging," *Magnetic Resonance in Medicine*, vol. 50, no. 3, pp. 560–569, Sep. 2003. [Online]. Available: https://onlinelibrary.wiley.com/doi/10.1002/mrm.10545

[29] E. Young, "APPLICATION OF MYELIN WATER IMAGING TO DETECT DIFFUSE WHITE MATTER DAMAGE IN MULTIPLE SCLEROSIS."

[30] A. L. MacKay and C. Laule, "Magnetic Resonance of Myelin Water: Anin vivo Marker for Myelin," *Brain Plasticity*, vol. 2, no. 1, pp. 71–91. [Online]. Available: https://www.ncbi.nlm.nih.gov/pmc/articles/PMC5928546/

[31] "Inversion recovery parameters." [Online]. Available: http://mriquestions.com/choice-of-ir-parameters.html

[32] D. Benjamini and P. Basser, "Towards clinically feasible relaxation-diffusion correlation MRI using MADCO," *Microporous and Mesoporous Materials*, vol. 269, Feb. 2017.

[33] L. J. ODonnell and C.-F. Westin, "An introduction to diffusion tensor image analysis," *Neurosurgery clinics of North America*, vol. 22, no. 2, pp. 185–viii, Apr. 2011. [Online]. Available: https://www.ncbi.nlm.nih.gov/pmc/articles/PMC3163395/

[34] "www.childrensmn.org-manuals-pfs-testproc-115956.pdf.png (552423)." [Online]. Available: https://www.childrensmn.org/educationmaterials/assets/img/www.childrensmn.org-manuals-pfs-testproc-115956.pdf.png

[35] T. J. Andrews, M. T. Osborne, and M. D. Does, "Diffusion of myelin water," *Magnetic Resonance in Medicine*, vol. 56, no. 2, pp. 381–385, Aug. 2006.

[36] "Solve nonlinear least-squares (nonlinear data-fitting) problems - MATLAB lsqnonlin - MathWorks Benelux." [Online]. Available: https://nl.mathworks.com/help/optim/ug/lsqnonlin.html

[37] J.-D. Tournier, S. Mori, and A. Leemans, "Diffusion tensor imaging and beyond," *Magnetic Resonance in Medicine*, vol. 65, no. 6, pp. 1532–1556, 2011, _eprint: https://onlinelibrary.wiley.com/doi/pdf/10.1002/mrm.22924. [Online]. Available: https://onlinelibrary.wiley.com/doi/abs/10.1002/mrm.22924

[38] "Shielded Cable: When To Use." [Online]. Available: https://www.wireandcabletips.com/importance-shielding-cabling/

[39] "Understanding Coaxial Cable." [Online]. Available: https://halberdbastion.com/resources/hardware/cables/understanding-coaxial-cable

[40] B. J. Wilm, C. Barmet, S. Gross, L. Kasper, S. J. Vannesjo, M. Haeberlin, B. E. Dietrich, D. O. Brunner, T. Schmid, and K. P. Pruessmann, "Single-shot spiral imaging enabled by an expanded encoding model: Demonstration in diffusion MRI," *Magnetic Resonance in Medicine*, vol. 77, no. 1, pp. 83–91, Jan. 2017.

[41] Y. Lee, B. J. Wilm, D. O. Brunner, S. Gross, T. Schmid, Z. Nagy, and K. P. Pruessmann, "On the signal-to-noise ratio benefit of spiral acquisition in diffusion MRI," *Magnetic Resonance in Medicine*, vol. 85, no. 4, pp. 1924–1937, Apr. 2021.

[42] S. Feizollah and C. L. Tardif, "High-resolution diffusion-weighted imaging at 7 Tesla: single-shot readout trajectories and their impact on signal-to-noise ratio, spatial resolution and accuracy," Jul. 2022, arXiv:2207.07778 [physics]. [Online]. Available: http://arxiv.org/abs/2207.07778

[43] C. Barmet, B. Wilm, M. Pavan, and K. Pruessmann, "A Third-Order Field Camera with Microsecond Resolution for MR System Diagnostics," *Proc Int Soc Magn Reson Med*, vol. 17, Jan. 2009.

[44] J. L. R. Andersson, M. S. Graham, I. Drobnjak, H. Zhang, and J. Campbell, "Susceptibility-induced distortion that varies due to motion: Correction in diffusion MR without acquiring additional data," *NeuroImage*, vol. 171, pp. 277–295, May 2018. [Online]. Available: https://www.sciencedirect.com/science/article/pii/S1053811917310601

[45] U. Rudrapatna, G. D. Parker, J. Roberts, and D. K. Jones, "A comparative study of gradient nonlinearity correction strategies for processing diffusion data obtained with ultra-strong gradient MRI scanners," *Magnetic Resonance in Medicine*, vol. 85, no. 2, pp. 1104–1113, 2021, _eprint: https://onlinelibrary.wiley.com/doi/pdf/10.1002/mrm.28464. [Online]. Available: https://onlinelibrary.wiley.com/doi/abs/10.1002/mrm.28464

[46] T. W. Redpath and F. W. Smith, "Technical note: use of a double inversion recovery pulse sequence to image selectively grey or white brain matter," *The British Journal of Radiology*, vol. 67, no. 804, pp. 1258–1263, Dec. 1994.

[47] J. R. Harrison, S. Bhatia, Z. X. Tan, A. Mirza-Davies, H. Benkert, C. M. W. Tax, and D. K. Jones, "Imaging Alzheimer's genetic risk using diffusion MRI: A systematic review," *NeuroImage. Clinical*, vol. 27, p. 102359, 2020.

[48] M. . Araque Caballero, M. Surez-Calvet, M. Duering, N. Franzmeier, T. Benzinger, A. M. Fagan, R. J. Bateman, C. R. Jack, J. Levin, M. Dichgans, M. Jucker, C. Karch, C. L. Masters, J. C. Morris, M. Weiner, M. Rossor, N. C. Fox, J.-H. Lee, S. Salloway, A. Danek, A. Goate, I. Yakushev, J. Hassenstab, P. R. Schofield, C. Haass, and M. Ewers, "White matter diffusion alterations precede symptom onset in autosomal dominant Alzheimer's disease," *Brain: A Journal of Neurology*, vol. 141, no. 10, pp. 3065–3080, Oct. 2018.

[49] R. Mito, D. Raffelt, T. Dhollander, D. N. Vaughan, J.-D. Tournier, O. Salvado, A. Brodtmann, C. C. Rowe, V. L. Villemagne, and A. Connelly, "Fibre-specific white matter reductions in Alzheimer's disease and mild cognitive impairment," *Brain: A Journal of Neurology*, vol. 141, no. 3, pp. 888–902, Mar. 2018.

[50] I. K. Amlien and A. M. Fjell, "Diffusion tensor imaging of white matter degeneration in Alzheimer's disease and mild cognitive impairment," *Neuroscience*, vol. 276, pp. 206–215, Sep. 2014.

[51] tsumpf, "tsumpf/arrShow," Jan. 2023, original-date: 2015-03-26T13:31:54Z. [Online]. Available: https://github.com/tsumpf/arrShow

[52] G. C. Ongko, "Iterated Reweighted Least Squares and GLMs Explained," Jul. 2022. [Online]. Available: https://towardsdatascience.com/iterated-reweighted-least-squares-and-glms-explained-9c0cc0063526